Science Advances
AAAS

advances.sciencemag.org/cgi/content/full/6/40/eaay9842/DC1

Supplementary Materials for

Wireless battery-free wearable sweat sensor powered by human motion

Yu Song, Jihong Min, You Yu, Haobin Wang, Yiran Yang, Haixia Zhang, Wei Gao*

*Corresponding author. Email: weigao@caltech.edu

Published 30 September 2020, *Sci. Adv.* **6**, eaay9842 (2020)
DOI: 10.1126/sciadv.aay9842

This PDF file includes:

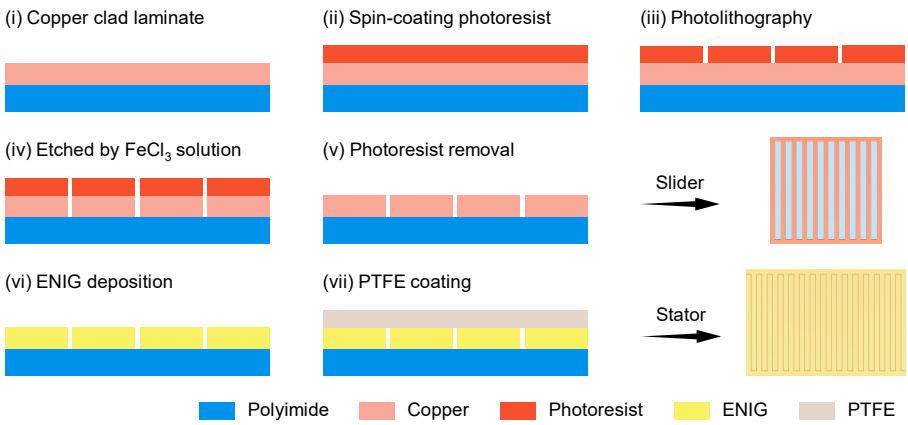

Fig. S1. Fabrication process of the slider and the stator of the FTENG. Steps (i-vi) are compatible to the commercial FPCB fabrication process.

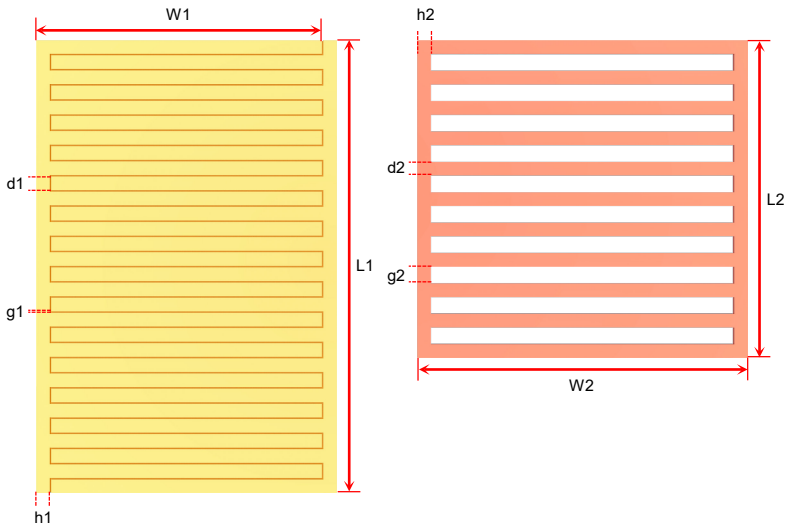

Dimension of FTENG

Stator	Length (mm)	Slider	Length (mm)
W1	37.8	W2	43.6
L1	59.8	L2	41.8
d1	1.8	d2	1.8
g1	0.2	g2	2.2
h1	1.8	h2	1.8

Fig. S2. Structure and parameters of the FPCB-based FTENG with an interdigital stator and a grating slider.

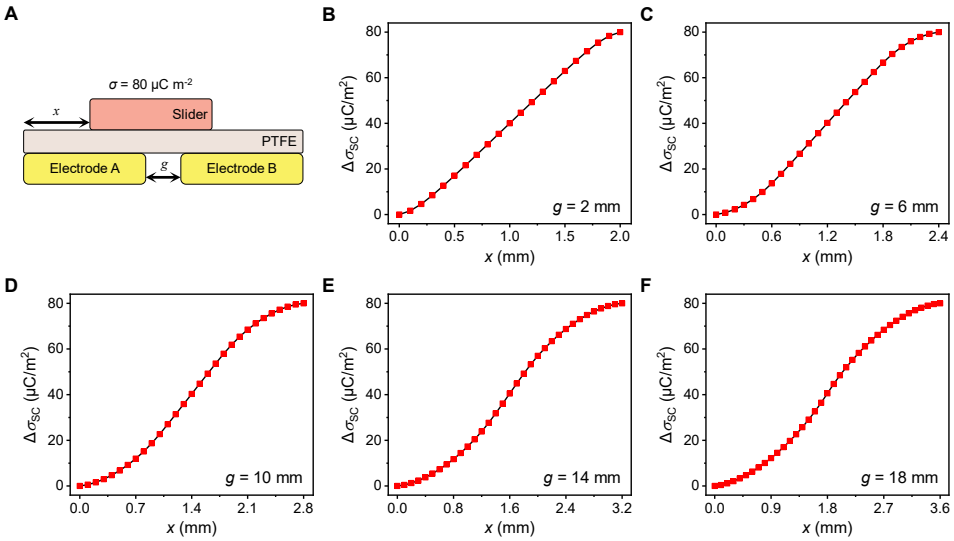

Fig. S3. Theoretical model and transferred charge density studies of FTENGs. (**A**) The theoretical model of FTENG. (**B**–**F**) The simulated transferred charge densities at different sliding displacements of 5 FTENGs with varied inter-electrode distances.

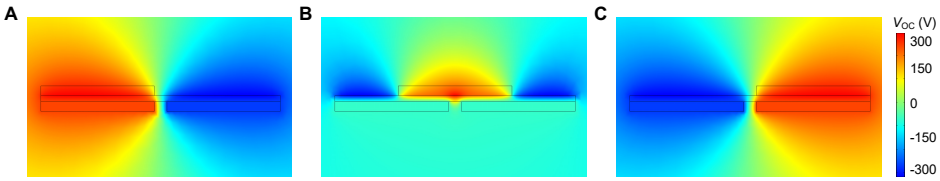

Fig. S4. Potential distribution across the interdigital electrodes of the FTENG under open-circuit condition. (**A**–**C**) The potential distributions at initial state (**A**), intermediate state (**B**), and final state (**C**), respectively, as simulated by COMSOL.

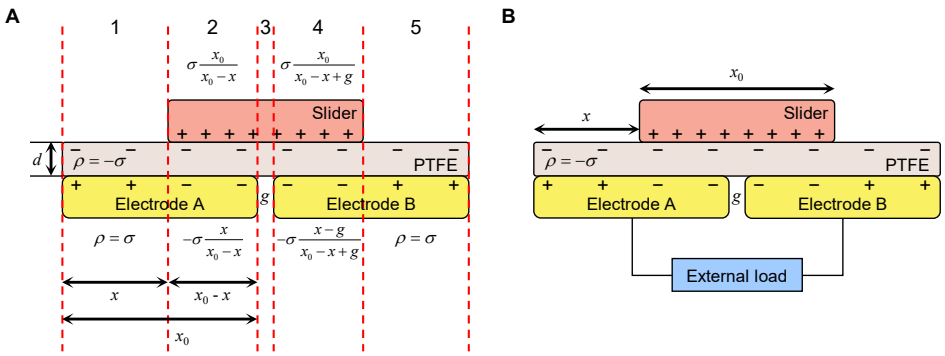

Fig. S5. Model and theoretical analysis of the FTENG. (**A** and **B**) Schematic illustration of FTENG under open-circuit condition (**A**) and short-circuit condition (**B**).

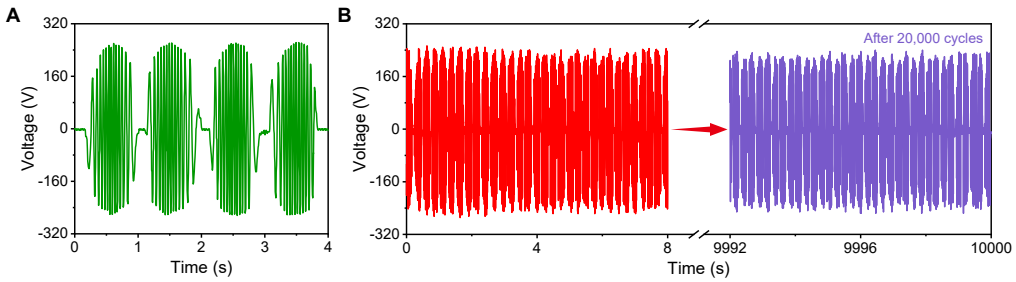

Fig. S6. Output performance of the FTENG. (**A**) Waveforms of output voltages of an FTENG under a working frequency of 0.5 Hz. (**B**) Cycling stability of output performance of a FTENG after 20,000 cycles under a working frequency of 2 Hz.

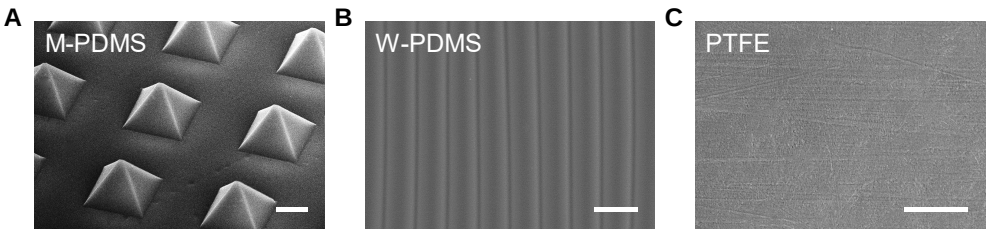

Fig. S7. Morphologies of different triboelectric materials before durability test. (**A**–**C**) Scanning electron microscopy (SEM) images of conventional micro-pyramid PDMS (M-PDMS) (**A**), wrinkled PDMS (W-PDMS) (**B**) and PTFE (**C**), respectively. Scale bars, 50 μm, 5 μm, and 50 μm, respectively.

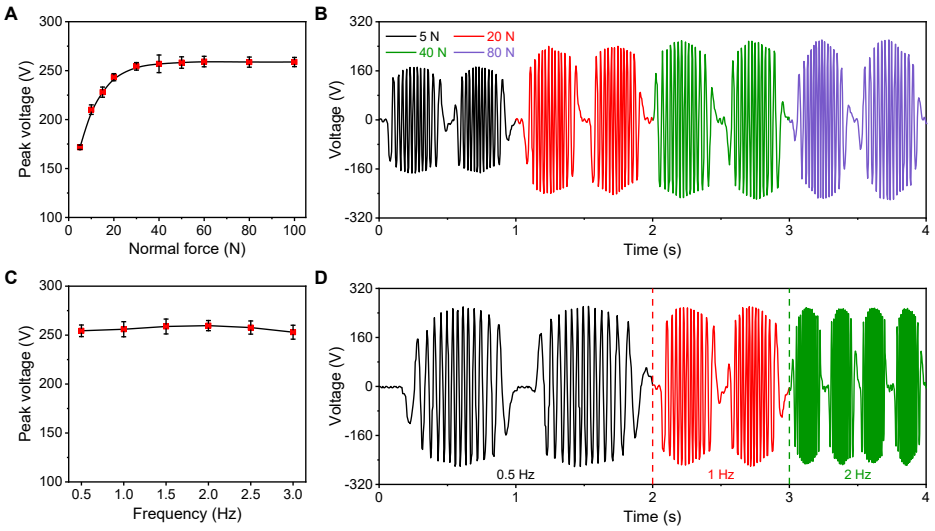

Fig. S8. Force-influenced performance of the FTENG. (**A**–**D**) The peak open-circuit voltage of the FTENG under different normal forces at a fixed working frequency of 1 Hz (**A** and **B**) and at varied working frequencies (**C** and **D**). The normal force acting on the FTENG was kept at 30 N for **C** and **D**. Error bars represent the standard deviations of the peak voltages measured from 10 working cycles.

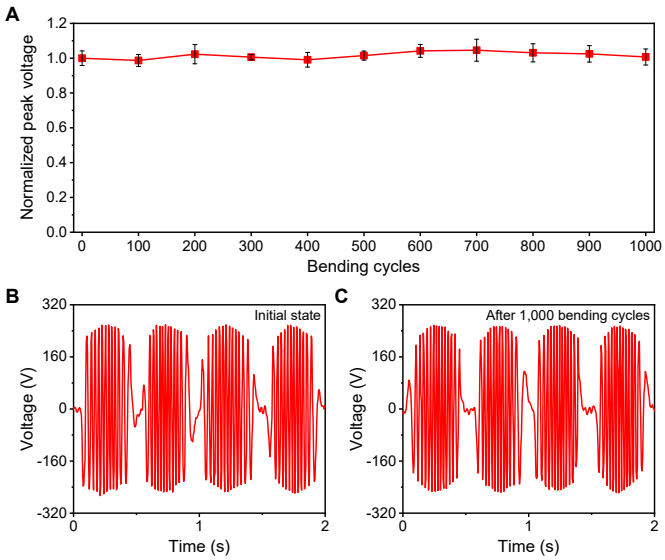

Fig. S9. Mechanical stability of the FTENG. (**A**) The normalized peak open-circuit voltage of an FTENG after hundreds of bending cycles at a working frequency of 1 Hz. (**B** and **C**) The output performance of an FTENG at initial state (**B**) and after 1,000 bending cycles (**C**) during the test. Error bar represents the standard deviations of the normalized peak voltages measured from 10 working cycles.

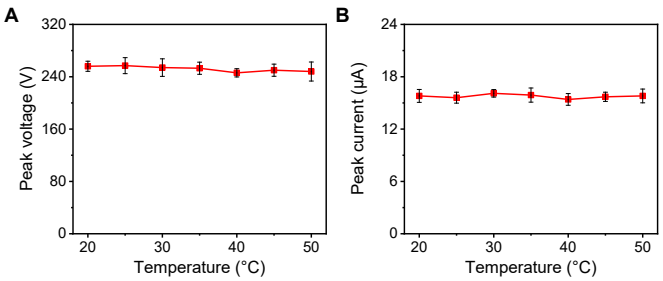

Fig. S10. Dependence of FTENG output on temperature. (**A** and **B**) Peak open-circuit voltage (**A**) and peak short-circuit current (**B**) of FTENG under different temperatures at a working frequency of 1 Hz. Error bars represent the standard deviations of the peak amplitudes measured from 10 working cycles.

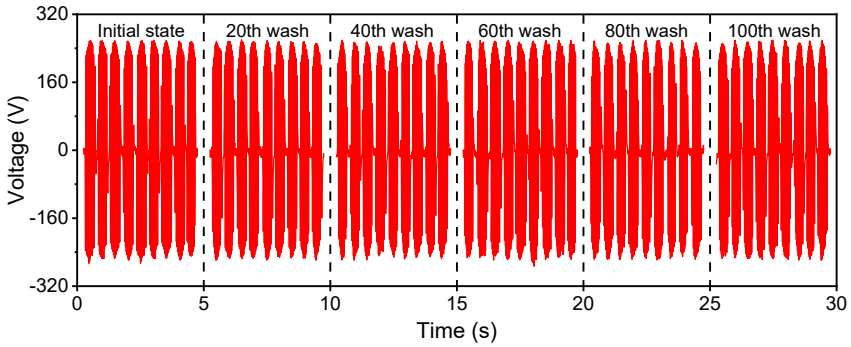

Fig. S11. Washing durability of the FTENG with 100 washing cycles at a working frequency of 1 Hz.

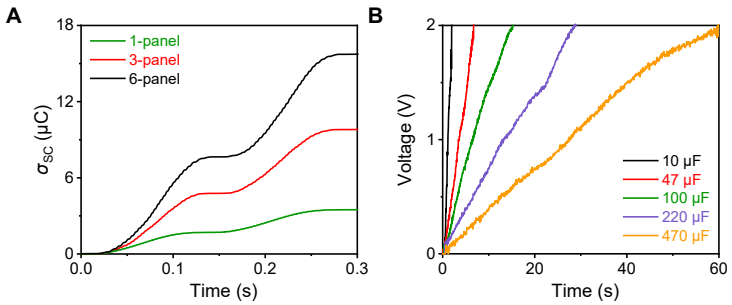

Fig. S12. Output performance of the FTENG with different panels. (**A**) Transferred charges of an FTENG with different panels during sliding process at a frequency of 3.3 Hz. (**B**) Charging curves of different capacitors charged to 2 V with a 3-panel FTENG through a rectifier at a working frequency of 2 Hz.

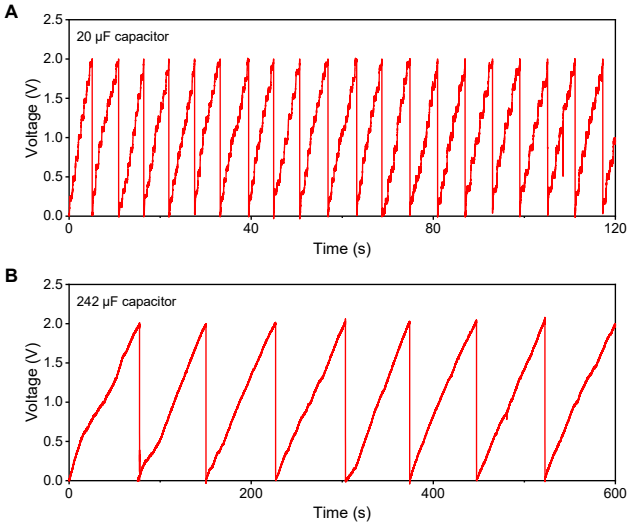

Fig. S13. Charging stability of the FTENG on different capacitors. (**A** and **B**) Charging curves of a 3-panel FTENG in charging a 20 μF (**A**) and 242 μF (**B**) capacitor under a working frequency of 1.5 Hz.

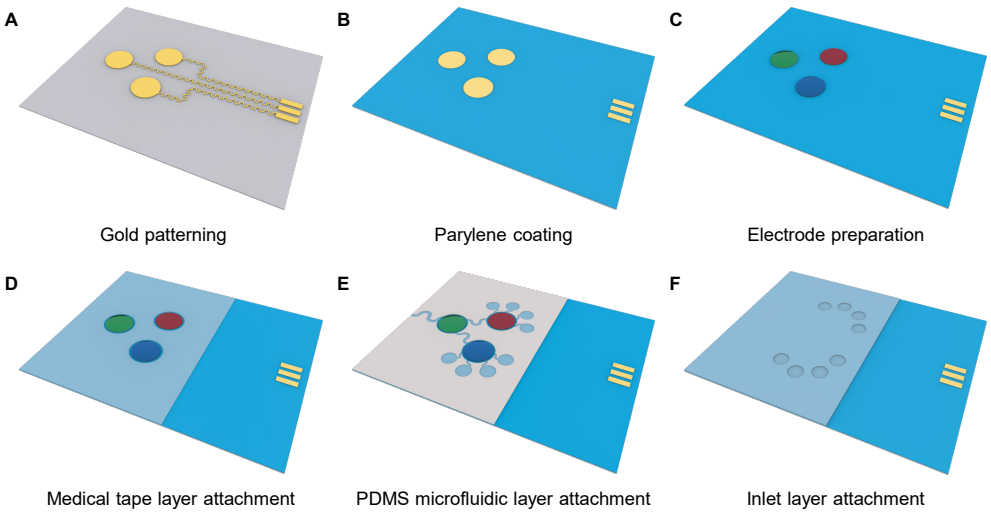

Fig. S14. Fabrication process of the microfluidic sensor patch. (**A**) Patterning of Au/Cr electrodes using photolithography, electron-beam evaporation and lift-off process on a PET substrate. (**B**) Patterning insulating layer *via* Parylene C deposition, photolithography and oxygen plasma etching. (**C**) Modifying working electrode and reference electrode through electrodeposition and drop casting. (**D**) Patterning laser-patterned medical tape. (**E**) Patterning the microfluidic channels in the PDMS layer. (**F**) Assembling medical tape with fluid inlets to form the microfluidic sensor patch.

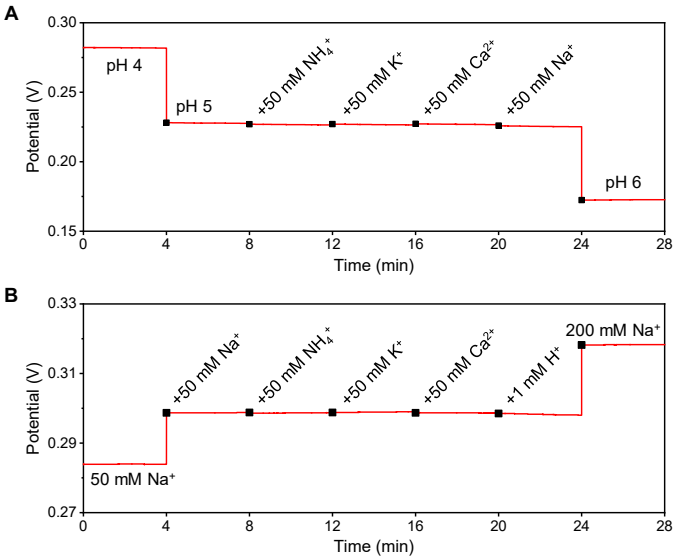

Fig. S15. Selectivity study of the biosensor array. (**A** and **B**) Selectivity study of a pH sensor (**A**) and a Na^+ sensor (**B**) against other major electrolytes in human sweat. Data recording was paused while changing solutions with 30 s waiting period.

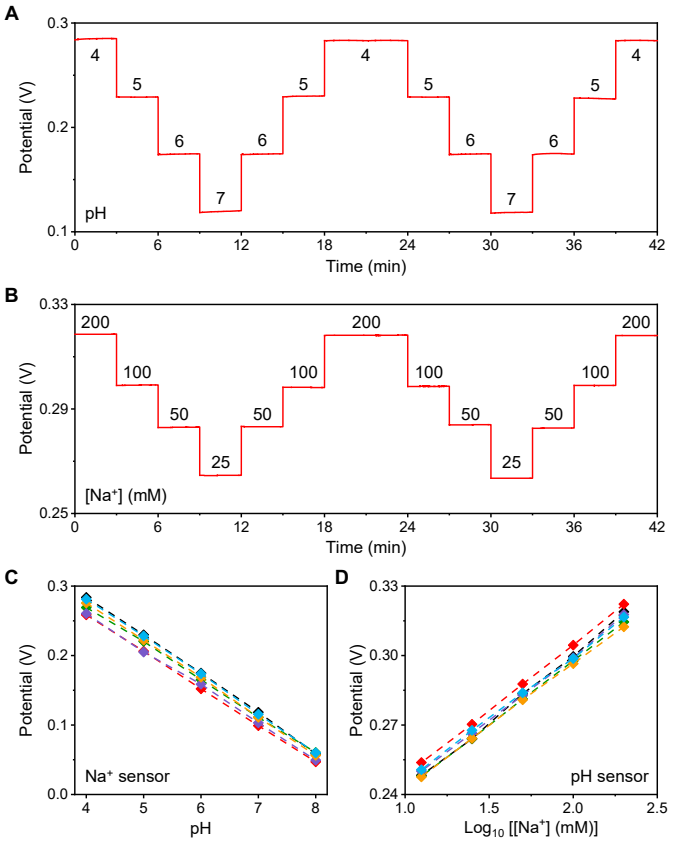

Fig. S16. Repeatability and reproducibility of the biosensor array. (**A** and **B**) Repeatability of a pH sensor in Mcilvaine's Buffer solutions (**A**) and a Na^+ sensor in NaCl solutions (**B**). (**C** and **D**) Reproducibility of pH sensors (**C**) and Na^+ sensors (**D**) (n=6).

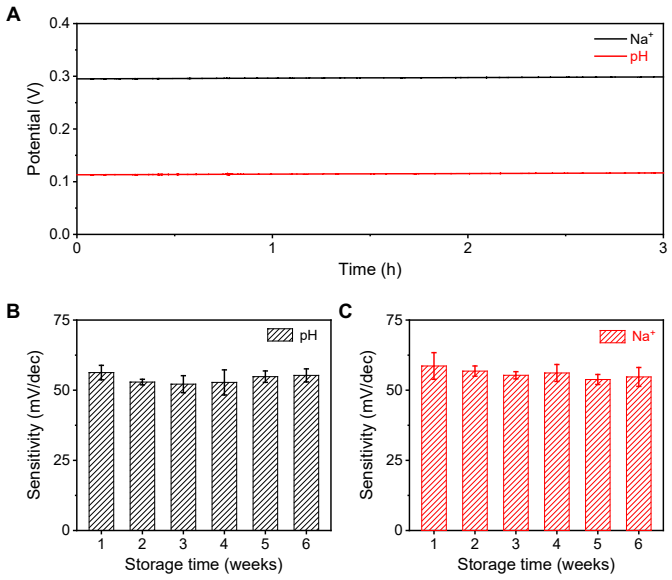

Fig. S17. Stability of the biosensor array. (**A**) Response stability of a pH sensor and a Na^+ sensor in a 100 mM NaCl solution for 3 h. (**B** and **C**) Long-term stability of pH sensors (**B**) and Na^+ sensors (**C**) after 6 weeks of storage. Error bars represent the standard deviation from 6 sensors.

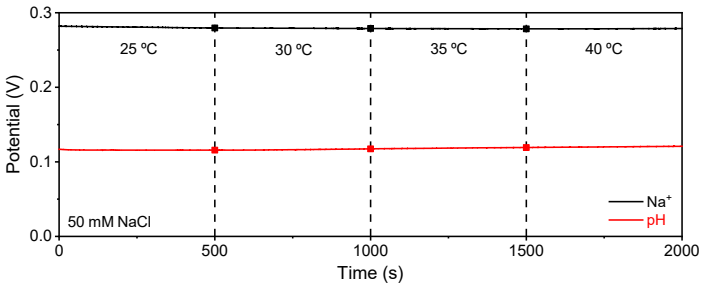

Fig. S18. Dependence of biosensor array on temperature.

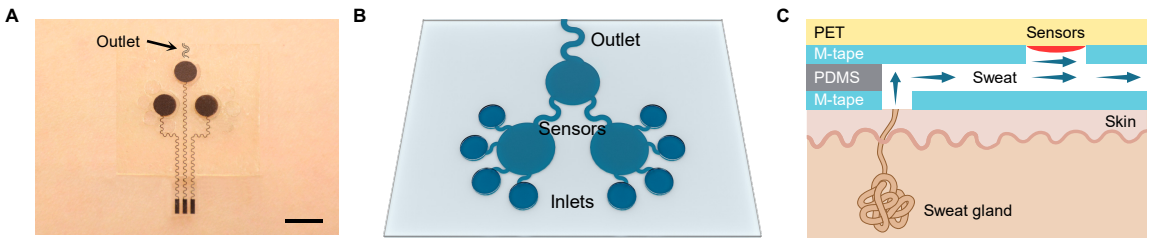

Fig. S19. Schematic of microfluidic design. (**A**) Optical image of a microfluidic sweat sensor patch. Scale bar, 5 mm. (**B**) Sweat flow in laser-engraved microfluidic channels. (**C**) Cross-section view of layout and operation of microfluidic sweat sensor patch. M-tape, medical tape. Photo credit: Yu Song, California Institute of Technology.

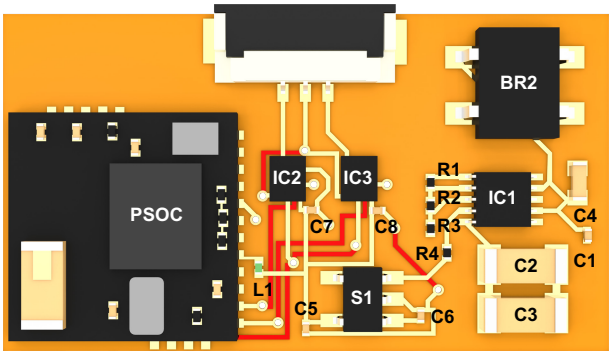

List of components

Components	Value and series number	Description
BR2	MB10S-13	Bridge Rectifier
C1	0.1 µF	0201 Capacitor
C2	220 µF	1206 Capacitor
C3	22 µF	1206 Capacitor
C4	10 µF	0402 Capacitor
C5	1 µF	0201 Capacitor
C6	1 µF	0201 Capacitor
C7	0.1 µF	0201 Capacitor
C8	0.1 µF	0201 Capacitor
L1	BKP0603HS121-T	0201 Ferrite Bead
IC1	S6AE101A	Energy Harvesting PMIC
IC2	AD8235ACBZ	Instrumentation Amplifier
IC3	AD8235ACBZ	Instrumentation Amplifier
PSOC	CYBLE-022001-00	EZ-BLE Module
S1	TPS7A0522PDBVT	LDO Regulator
R1	5.6 MΩ	0201 Resistor
R2	4.3 MΩ	0201 Resistor
R3	7.5 MΩ	0201 Resistor
R4	10 Ω	0201 Resistor

Fig. S20. Schematic and list of components of the flexible circuitry.

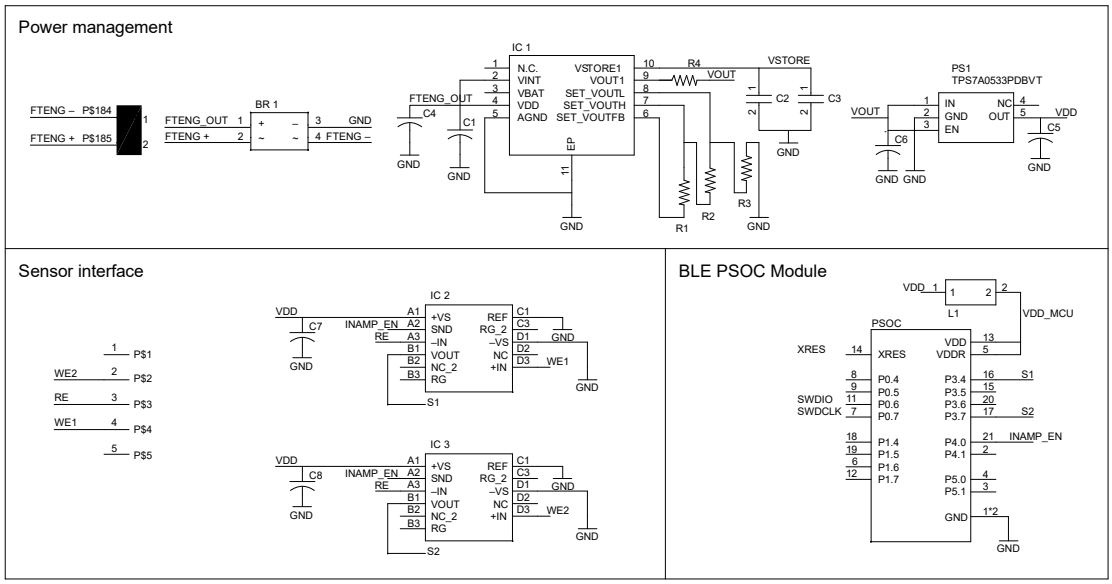

Fig. S21. Circuit diagram of power management, sensor interface, and BLE PSoC modules.

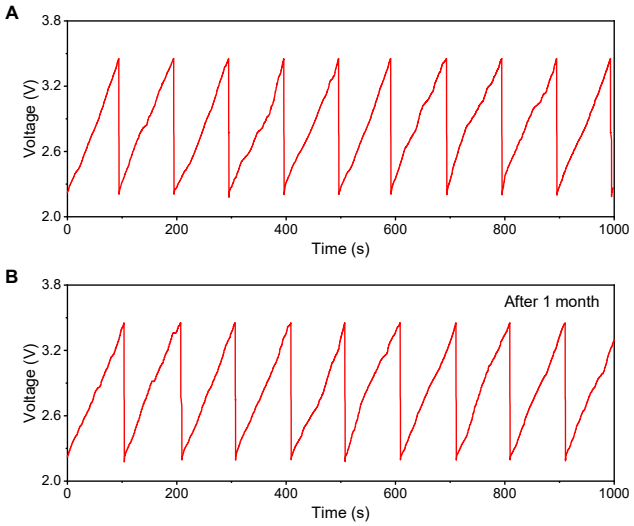

Fig. S22. Long-term stability of FWS^3. (**A** and **B**) Charging curves of the capacitor when an FWS^3 operates under a working frequency of 1.5 Hz before (**A**) and after 1 month (**B**).

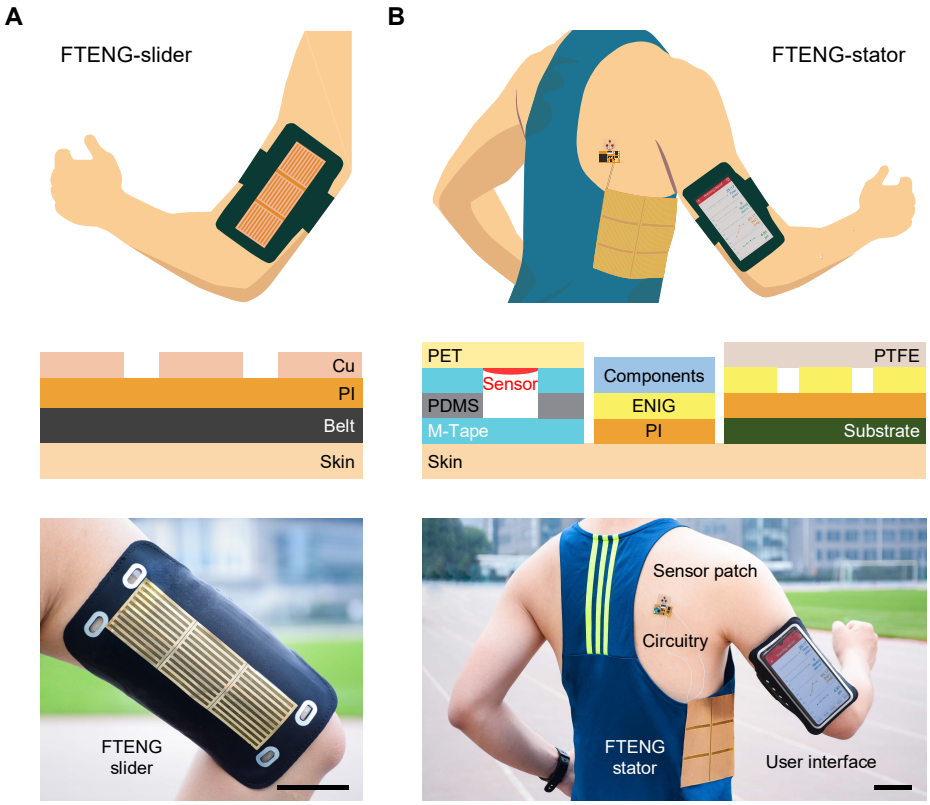

Fig. S23. Schematic and optical images of an FTENG worn on body. (**A** and **B**) Schematic, cross-section view and real photos of FTENG slider (**A**) and FTENG stator (**B**) worn on body. Scale bars, 5 cm. Photo credit: Yu Song, California Institute of Technology.

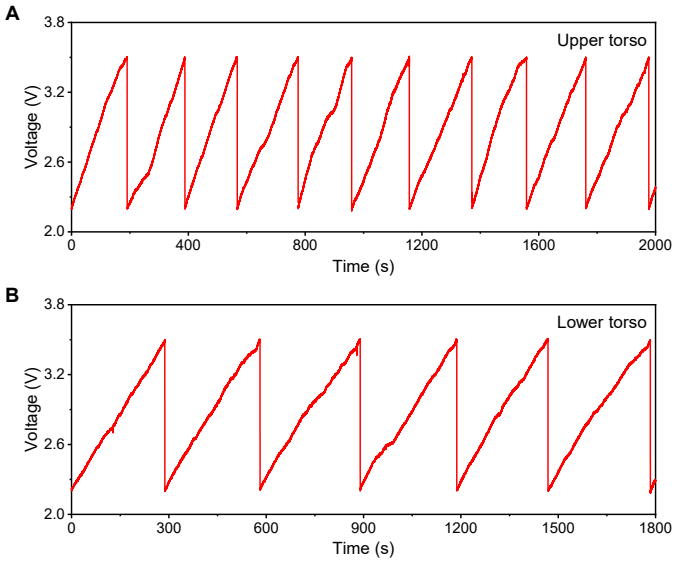

Fig. S24. Real-time potential of the circuitry capacitor charged by an FTENG. (**A** and **B**) The circuitry capacitor charged by an FTENG at different positions (**A**) and different contact modes (**B**) during a regular running of a healthy subject.

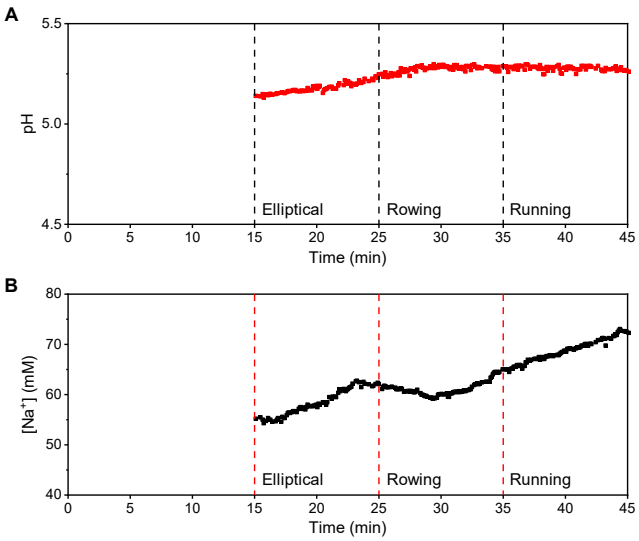

Fig. S25. Real-time sweat pH and Na^+ level wirelessly obtained from an FWS^3 during different physical exercises. In this experiment, the FWS^3 system was charged by a battery instead to collect continuous data points for better noise characterization.

Note S1. Model and theoretical analysis of the FTENG under open-circuit condition

Typically, this freestanding triboelectric nanogenerator is composed of a slider, an interdigital stator and a dielectric film, where a copper slider attached on the PTFE-laminated electrodes. Due to the different ability to gain electrons, there will be positive charges on the slider (copper) and negative charges on the surface of PTFE dielectric film according to the triboelectric series.

In the open-circuit condition (**fig. S5A**), electrons cannot transfer between two interdigital electrodes. The open-circuit voltage is defined as the electric potential difference, that is $V_{OC}=U_A-U_B$. On the basis of the assumption that the thickness of the PTFE is far smaller than its width dimension, an analytical model can be presented where the overlapped region between the slider and the electrodes can be treated as a parallel-plate capacitor without the edge effect involved.

With the triboelectric charge density of $-\sigma$ on the PTFE surface, the non-overlapped regions on electrode A and electrode B (regions 1 and 5) show an induced charge density of σ. Assumed that the no net charges on electrodes in open-circuit condition, the induced charge density on overlapped region (region 2 and 4) can be expressed as

$$\rho_{2A} = -\sigma \frac{x}{x_0 - x} \tag{S1}$$

$$\rho_{4B} = -\sigma \frac{x - g}{x_0 - x + g} \tag{S2}$$

where x_0 represents the width of slider and electrode of stator, x represents the sliding distance from the initial position, and g represents the gap between two interdigital electrodes of stator, respectively.

Based on the law of conservation of charge, the charge density on different regions of slider can be expressed as

$$\rho_{2S} = \sigma + \sigma \frac{x}{x_0 - x} = \sigma \frac{x_0}{x_0 - x} \tag{S3}$$

$$\rho_{4S} = \sigma + \sigma \frac{x - g}{x_0 - x + g} = \sigma \frac{x_0}{x_0 - x + g} \tag{S4}$$

The electric field within PTFE film for region 2 and 4 can be expressed as

$$E_2 = -\frac{\sigma}{\varepsilon_0 \varepsilon_r} \frac{x}{x_0 - x} \tag{S5}$$

$$E_4 = -\frac{\sigma}{\varepsilon_0 \varepsilon_r} \frac{x - g}{x_0 - x + g} \tag{S6}$$

where ε_0 is the dielectric constant of the vacuum, and ε_r is the relative dielectric constant of PTFE, respectively.

Then the potential difference between the slider with two electrodes can be expressed as

$$U_S - U_A = \frac{d \cdot \sigma}{\varepsilon_0 \varepsilon_r} \cdot \frac{x}{x_0 - x} \tag{S7}$$

$$U_S - U_B = \frac{d \cdot \sigma}{\varepsilon_0 \varepsilon_r} \cdot \frac{x - g}{x_0 - x + g} \tag{S8}$$

where d is the thickness of PTFE film.

The slider is an equipotential body, thus the potential difference between two electrodes (V_{OC}) can be expressed as

$$V_{OC} = U_A - U_B = \frac{d \cdot \sigma}{\varepsilon_0 \varepsilon_r} \cdot \frac{x - g}{x_0 - x + g} - \frac{d \cdot \sigma}{\varepsilon_0 \varepsilon_r} \cdot \frac{x}{x_0 - x} = \frac{d \cdot \sigma}{\varepsilon_0 \varepsilon_r} \cdot \left(\frac{x - g}{x_0 - x + g} - \frac{x}{x_0 - x} \right) \tag{S9}$$

Specifically, when x approaches 0, g, x_0, and $x_0 + g$, only small overlapped area occurred with electrode and the assumption of parallel-plate capacitor is not applicable anymore. Therefore, it is essential to derivate the V_{OC} at initial and final positions.

At initial state ($x = 0$), where the slider fully overlaps with electrode A, the charge density at the contact interface of electrode A and electrode B is σ and $-\sigma$, respectively. Then the electrical potential of electrode A and electrode B with an infinitely far position as zero-potential reference can be expressed as

$$U_A = \frac{d \cdot \sigma}{\varepsilon_0 \varepsilon_r} \tag{S10}$$

$$U_B = -\frac{d \cdot \sigma}{\varepsilon_0 \varepsilon_r} \tag{S11}$$

Thus, V_{OCI} at the initial state is

$$V_{OCI} = U_A - U_B = 2 \cdot \frac{d \cdot \sigma}{\varepsilon_0 \varepsilon_r} \tag{S12}$$

With same derivation, the V_{OCF} at the final state ($x = x_0 + g$) can be expressed as

$$V_{OCF} = U_A - U_B = -2 \cdot \frac{d \cdot \sigma}{\varepsilon_0 \varepsilon_r} \tag{S13}$$

Therefore, the peak-to-peak value of V_{OC} is

$$V_{OC} = V_{OCI} - V_{OCF} = 4 \cdot \frac{d \cdot \sigma}{\varepsilon_0 \varepsilon_r} \tag{S14}$$

Note S2. Model and theoretical analysis of the FTENG under short-circuit condition

The basic model of FTENG in short-circuit condition with external load is shown in **fig. S5B**, where all layers own an in-plane length *w*. Assumed that only a small region of *dx* in PTFE film surface contains the triboelectric charges with the density of σ, the correspondingly total charges on electrode A and electrode B are σwdk. The total charges on electrode A and electrode B in short-circuit condition can be expressed as

$$dQ_A = \frac{\sigma \cdot w \cdot dx}{1+\frac{C_B(x)}{C_A(x)}} \tag{S15}$$

$$dQ_B = \frac{\sigma \cdot w \cdot dx}{1+\frac{C_A(x)}{C_B(x)}} \tag{S16}$$

where $C_i(x)$ represents the capacitance between this small surface and electrode *i*.
Because of the superposition principle of electrostatic field, the total charge of two electrodes can be obtained by integration

$$Q_A = \sigma \cdot w \int_0^{x_0} \frac{dx}{1+\frac{C_B(x)}{C_A(x)}} \tag{S17}$$

$$Q_B = \sigma \cdot w \int_0^{x_0} \frac{dx}{1+\frac{C_A(x)}{C_B(x)}} \tag{S18}$$

The transferred charge (Q_{SC}) in short-circuit condition can be shown as

$$Q_{SC} = Q_B - Q_A = \int_0^{x_0} \frac{\sigma \cdot w \cdot dx}{1+\left(\frac{C_A(x)}{C_B(x)}\right)_{x=x_0+g}} - \int_0^{x_0} \frac{\sigma \cdot w \cdot dx}{1+\left(\frac{C_B(x)}{C_A(x)}\right)_{x=0}} \tag{S19}$$

When $x = 0$, the PTFE film is much closer to electrode A than electrode B, and the ratio $C_B(x)/C_A(x)$ is close to 0. Then Q_A will be approximately $\sigma w x_0$ and Q_B will be approximately 0.

When $x = g + x_0$, the ratio $C_B(x)/C_A(x)$ is close to infinity, and Q_A will be approximately 0 and Q_B will be approximately $\sigma w x_0$.

Therefore, Q_{SC} can reach $\sigma w x_0$ during the one sliding process. The change of the ratio of these two capacitances with the change of *x* is the core-working principle of FTENG.

Table S1. Comparison of currently reported wearable TENGs.

Working Mode	Size (cm^2)	Material preparation	Position	Output	Power density	Sampling rate	Durability	Washability	Ref.
Contact-separation	4 * 4	Weaving process	Wrist	150 V, 1.5μA	85 mW m^{-2}	1 – 5 Hz	50,000	Washable	41
Contact-separation	6 * 4	Weaving process	Waist	4.98 V, 37.2 μA	33.16 mW m^{-2}	0.4 Hz	1,000	Washable	42
Contact-separation	4.5 * 4	Weaving process	Arm	45 V, 9.9 μA	263.36 mW m^{-2}	0.5 – 5 Hz	1,500	Washable	43
Contact-separation	6 * 8	Weaving process	Hand	206 V, 1.5 μA	30.4 mW m^{-2}	1 Hz	10,000	Washable	44
Contact-separation	1.4	Inkjet printing	Shoe	54.8 V, 1.2 μA	126 mW m^{-2}	0.75 – 4 Hz	500	N/A	45
Lateral-sliding	2 * 5	ICP etching	Knee	24.1 V	N/A	0.7 Hz	1,000	N/A	46
Single-electrode	4.5 * 10.5	Drop coating	Arm	70 V, 28.35 μA	500 mW m^{-2}	1 – 4 Hz	3,600	N/A	47
Single-electrode	6 * 3	Blade coating	Wrist	180 V, 22.6 μA	4.06 mW m^{-2}	0.5 – 2.5 Hz	200	N/A	48
Freestanding	12 * 8	Weaving process	Side torso	118 V, 1.5 μA	N/A	1 – 5 Hz	15,000	N/A	49
Freestanding	5.78 * 3.78	FPCB technique	Side torso	248 V, 42.3 μA	415.9 mW m^{-2}	0.5 – 3.3 Hz	20,000	Washable	This work

Table S2. Comparison of TENG-powered wireless sensor systems.

Power source	Working mode	Working condition	Charging period	External power	Sensing signal	Data	Wearable	Ref.
Air flow	Freestanding	100 μF, 8 V	N/A	Yes	Wind speed	Bluetooth	No	50
Air/water flow	Contact-separation	1 mF, 5 V	40 min	No	pH	Bluetooth	No	51
Air flow	Freestanding	10 mF, 3.3 V	98 s	No	Temperature	RF transmission	No	52
Water flow	Freestanding	1 mF, 3.3 V	60 min	No	Temperature	RF transmission	No	53
Air flow/light	Contact-separation	100 mAh, 2.7 V	540 s	No	Temperature	RF transmission	No	54
Human motion	Freestanding	N/A	45 min	No	Heart rate	Bluetooth	Yes	55
Human motion	Contact-separation	N/A	N/A	Yes	Ca^{2+}	RF transmission	Yes	56
Human motion	Freestanding	242 μF, 3.5 V	60 s	No	pH & Na^{2+}	Bluetooth	Yes	This work

REFERENCES AND NOTES

1. J. Kim, A. S. Campbell, B. E.-F. de Ávila, J. Wang, Wearable biosensors for healthcare monitoring. *Nat. Biotechnol.* **37**, 389–406 (2019).

2. T. R. Ray, J. Choi, A. J. Bandodkar, S. Krishnan, P. Gutruf, L. Tian, R. Ghaffari, J. A. Rogers, Bio-integrated wearable systems: A comprehensive review. *Chem. Rev.* **119**, 5461–5533 (2019).

3. T. Someya, Z. Bao, G. G. Malliaras, The rise of plastic bioelectronics. *Nature* **540**, 379–385 (2016).

4. Y. Yang, W. Gao, Wearable and flexible electronics for continuous molecular monitoring. *Chem. Soc. Rev.* **48**, 1465–1491 (2019).

5. D.-H. Kim, N. Lu, R. Ma, Y.-S. Kim, R.-H. Kim, S. Wang, J. Wu, S. M. Won, H. Tao, A. Islam, K. J. Yu, T.-i. Kim, R. Chowdhury, M. Ying, L. Xu, M. Li, H.-J. Chung, H. Keum, M. M. Cormick, P. Liu, Y.-W. Zhang, F. G. Omenetto, Y. Huang, T. Coleman, J. A. Rogers, Epidermal electronics. *Science* **333**, 838–843 (2011).

6. D. Son, J. Kang, O. Vardoulis, Y. Kim, N. Matsuhisa, J. Y. Oh, J. W. F. To, J. Mun, T. Katsumata, Y. Liu, A. F. Mc Guire, M. Krason, F. Molina-Lopez, J. Ham, U. Kraft, Y. Lee, Y. Yun, J. B.-H. Tok, Z. Bao, An integrated self-healable electronic skin system fabricated via dynamic reconstruction of a nanostructured conducting network. *Nat. Nanotechnol.* **13**, 1057–1065 (2018).

7. Q. Hua, J. Sun, H. Liu, R. Bao, R. Yu, J. Zhai, C. Pan, Z. L. Wang, Skin-inspired highly stretchable and conformable matrix networks for multifunctional sensing. *Nat. Commun.* **9**, 244 (2018).

8. C. Wang, X. Li, H. Hu, L. Zhang, Z. Huang, M. Lin, Z. Zhang, Z. Yin, B. Huang, H. Gong, S. Bhaskaran, Y. Gu, M. Makihata, Y. Guo, Y. Lei, Y. Chen, C. Wang, Y. Li, T. Zhang, Z. Chen, A. P. Pisano, L. Zhang, Q. Zhou, S. Xu, Monitoring of the central blood pressure waveform via a conformal ultrasonic device. *Nat. Biomed. Eng.* **2**, 687–695 (2018).

9. H.-R. Lim, H. S. Kim, R. Qazi, Y.-T. Kwon, J.-W. Jeong, W.-H. Yeo, Advanced soft materials, sensor integrations, and applications of wearable flexible hybrid electronics in healthcare, energy, and environment. *Adv. Mater.* **32**, 1901924 (2020).

10. W. Gao, S. Emaminejad, H. Y. Y. Nyein, S. Challa, K. Chen, A. Peck, H. M. Fahad, H. Ota, H. Shiraki, D. Kiriya, D.-H. Lien, G. A. Brooks, R. W. Davis, A. Javey, Fully integrated wearable sensor arrays for multiplexed *in situ* perspiration analysis. *Nature* **529**, 509–514 (2016).

11. H. Lee, T. K. Choi, Y. B. Lee, H. R. Cho, R. Ghaffari, L. Wang, H. J. Choi, T. D. Chung, N. Lu, T. Hyeon, S. H. Choi, D.-H. Kim, A graphene-based electrochemical device with thermoresponsive microneedles for diabetes monitoring and therapy. *Nat. Nanotechnol.* **11**, 566–572 (2016).

12. A. Koh, D. Kang, Y. Xue, S. Lee, R. M. Pielak, J. Kim, T. Hwang, S. Min, A. Banks, P. Bastien, M. C. Manco, L. Wang, K. R. Ammann, K.-I. Jang, P. Won, S. Han, R. Ghaffari, U. Paik, M. J. Slepian, G. Balooch, Y. Huang, J. A. Rogers, A soft, wearable microfluidic device for the capture, storage, and colorimetric sensing of sweat. *Sci. Transl. Med.* **8**, 366ra165 (2016).

13. Y. Yang, Y. Song, X. Bo, J. Min, O. S. Pak, L. Zhu, M. Wang, J. Tu, A. Kogan, H. Zhang, T. K. Hsiai, Z. Li, W. Gao, A laser-engraved wearable sensor for sensitive detection of uric acid and tyrosine in sweat. *Nat. Biotechnol.* **38**, 217–224 (2020).

14. M. Bariya, H. Y. Y. Nyein, A. Javey, Wearable sweat sensors. *Nat. Electron.* **1**, 160–171 (2018).

15. R. M. Torrente-Rodríguez, J. Tu, Y. Yang, J. Min, M. Wang, Y. Song, Y. Yu, C. Xu, C. Ye, W. W. IsHak, W. Gao, Investigation of cortisol dynamics in human sweat using a graphene-based wireless mHealth system. *Matter* **2**, 921–937 (2020).

16. H. Lee, C. Song, Y. S. Hong, M. S. Kim, H. R. Cho, T. Kang, K. Shin, S. H. Choi, T. Hyeon, D.-H. Kim, Wearable/disposable sweat-based glucose monitoring device with multistage transdermal drug delivery module. *Sci. Adv.* **3**, e1601314 (2017).

17.. Choi, R. Ghaffari, L. B. Baker, J. A. Rogers, Skin-interfaced systems for sweat collection and analytics. *Sci. Adv.* **4**, eaar3921 (2018).

18. S. Emaminejad, W. Gao, E. Wu, Z. A. Davies, H. Y. Y. Nyein, S. Challa, S. P. Ryan, H. M. Fahad, K. Chen, Z. Shahpar, S. Talebi, C. Milla, A. Javey, R. W. Davis, Autonomous sweat extraction and analysis applied to cystic fibrosis and glucose monitoring using a fully integrated wearable platform. *Proc. Natl. Acad. Sci. U.S.A.* **114**, 4625–4630 (2017).

19. A. J. Bandodkar, W. J. Jeang, R. Ghaffari, J. A. Rogers, Wearable sensors for biochemical sweat analysis. *Annu. Rev. Anal. Chem.* **12**, 1–22 (2019).

20. M. C. Brothers, M. DeBrosse, C. C. Grigsby, R. R. Naik, S. M. Hussain, J. Heikenfeld, S. S. Kim, Achievements and challenges for real-time sensing of analytes in sweat within wearable platforms. *Acc. Chem. Res.* **52**, 297–306 (2019).

21. W. He, C. Wang, H. Wang, M. Jian, W. Lu, X. Liang, X. Zhang, F. Yang, Y. Zhang, Integrated textile sensor patch for real-time and multiplex sweat analysis. *Sci. Adv.* **5**, eaax0649 (2019).

22. . A. M. Zamarayeva, A. E. Ostfeld, M. Wang, J. K. Duey, I. Deckman, B. P. Lechêne, G. Davies, D. A. Steingart, A. C. Arias, Flexible and stretchable power sources for wearable electronics. *Sci. Adv.* **3**, e1602051 (2017).

23. J. Li, J. Zhao, J. A. Rogers, Materials and designs for power supply systems in skin-interfaced electronics. *Acc. Chem. Res.* **52**, 53–62 (2019).

24. A. J. Bandodkar, P. Gutruf, J. Choi, K. H. Lee, Y. Sekine, J. T. Reeder, W. J. Jeang, A. J. Aranyosi, S. P. Lee, J. B. Model, R. Ghaffari, C.-J. Su, J. P. Leshock, T. Ray, A. Verrillo, K. Thomas, V. Krishnamurthi, S. Han, J. Kim, S. Krishnan, T. Hang, J. A. Rogers, Battery-free, skin-interfaced microfluidic/electronic systems for simultaneous electrochemical, colorimetric, and volumetric analysis of sweat. *Sci. Adv.* **5**, eaav3294 (2019).

25. J. T. Reeder, J. Choi, Y. Xue, P. Gutruf, J. Hanson, M. Liu, T. Ray, A. J. Bandodkar, R. Avila, W. Xia, S. Krishnan, S. Xu, K. Barnes, M. Pahnke, R. Ghaffari, Y. Huang, J. A. Rogers, Waterproof, electronics-enabled, epidermal microfluidic devices for sweat collection, biomarker analysis, and thermography in aquatic settings. *Sci. Adv.* **5**, eaau6356 (2019).

26. J. Zhao, Y. Lin, J. Wu, H. Y. Y. Nyein, M. Bariya, L. C. Tai, M. Chao, W. Ji, G. Zhang, Z. Fan, A. Javey, A fully integrated and self-powered smartwatch for continuous sweat glucose monitoring. *ACS Sens.* **4**, 1925–1933 (2019).

27. S. Park, S. W. Heo, W. Lee, D. Inoue, Z. Jiang, K. Yu, H. Jinno, D. Hashizume, M. Sekino, T. Yokota, K. Fukuda, K. Tajima, T. Someya, Self-powered ultra-flexible electronics via nano-grating-patterned organic photovoltaics. *Nature* **561**, 516–521 (2018).

28. G. Chen, Y. Li, M. Bick, J. Chen, Smart textiles for electricity generation. *Chem. Rev.* **8**, 3668–3720 (2020).

29. A. J. Bandodkar, J.-M. You, N.-H. Kim, Y. Gu, R. Kumar, A. M. V. Mohan, J. Kurniawan, S. Imani, T. Nakagawa, B. Parish, M. Parthasarathy, P. P. Mercier, S. Xu, J. Wang, Soft, stretchable, high power density electronic skin-based biofuel cells for scavenging energy from human sweat. *Energy Environ. Sci.* **10**, 1581–1589 (2017).

30. F.-R. Fan, Z.-Q. Tian, Z. L. Wang, Flexible triboelectric generator. *Nano Energy* **1**, 328–334 (2012).

31. W. Seung, M. K. Gupta, K. Y. Lee, K.-S. Shin, J.-H. Lee, T. Y. Kim, S. Kim, J. Lin, J. H. Kim, S.-W. Kim, Nanopatterned textile-based wearable triboelectric nanogenerator. *ACS Nano* **9**, 3501–3509 (2015).

32. J. Chen, Y. Huang, N. Zhang, H. Zou, R. Liu, C. Tao, X. Fan, Z. L. Wang, Micro-cable structured textile for simultaneously harvesting solar and mechanical energy. *Nat. Energy* **1**, 16138 (2016).

33. J. Wang, S. Li, F. Yi, Y. Zi, J. Lin, X. Wang, Y. Xu, Z. L. Wang, Sustainably powering wearable electronics solely by biomechanical energy. *Nat. Commun.* **7**, 12744 (2016).

34. X. Pu, M. Liu, X. Chen, J. Sun, C. Du, Y. Zhang, J. Zhai, W. Hu, Z. L. Wang, Ultrastretchable, transparent triboelectric nanogenerator as electronic skin for biomechanical energy harvesting and tactile sensing. *Sci. Adv.* **3**, e1700015 (2017).

35. D. Liu, X. Yin, H. Guo, L. Zhou, X. Li, C. Zhang, J. Wang, Z. L. Wang, A constant current triboelectric nanogenerator arising from electrostatic breakdown. *Sci. Adv.* **5**, eaav6437 (2019).

36. Z. Liu, H. Li, B. Shi, Y. Fan, Z. L. Wang, Z. Li, Wearable and implantable triboelectric nanogenerators. *Adv. Funct. Mater.* **29**, 1808820 (2019).

37. S. S. Kwak, H.-J. Yoon, S.-W. Kim, Textile-based triboelectric nanogenerators for self-powered wearable electronics. *Adv. Funct. Mater.* **29**, 1804533 (2019).

38. X. Chen, Y. Song, Z. Su, H. Chen, X. Cheng, J. Zhang, M. Han, H. Zhang, Flexible fiber-based hybrid nanogenerator for biomechanical energy harvesting and physiological monitoring, *Nano Energy* **38**, 43–50 (2017).

39. Y. Song, H. Wang, X. Cheng, G. Li, X. Chen, H. Chen, L. Miao, H. Zhang, High-efficiency self-charging smart bracelet for portable electronics, *Nano Energy* **55**, 29–36 (2019).

40. C. J. de Ruiter, P. W. L. Verdijk, W. Werker, M. J. Zuidema, A. de Haan, Stride frequency in relation to oxygen consumption in experienced and novice runners. *Eur. J. Sport Sci.* **14**, 251–258 (2014).

41. K. Dong, Y.-C. Wang, J. Deng, Y. Dai, S. L. Zhang, H. Zou, B. Gu, B. Sun, Z. L. Wang, A highly stretchable and washable all-yarn-based self-charging knitting power textile composed of fiber triboelectric nanogenerators and supercapacitors. *ACS Nano* **11**, 9490–9499 (2017).

42. Z. Zhao, C. Yan, Z. Liu, X. Fu, L.-M. Peng, Y. Hu, Z. Zheng, Machine-washable textile triboelectric nanogenerators for effective human respiratory monitoring through loom weaving of metallic yarns. *Adv. Mater.* **28**, 10267–10274 (2016).

43. K. Dong, J. Deng, Y. Zi, Y.-C. Wang, C. Xu, H. Zou, W. Ding, Y. Dai, B. Gu, B. Sun, Z. L. Wang, 3D orthogonal woven triboelectric nanogenerator for effective biomechanical energy harvesting and as self-powered active motion sensors. *Adv. Mater.* **29**, 1702648 (2017).

44. W. Wang, A. Yu, X. Liu, Y. Liu, Y. Zhang, Y. Zhu, Y. Lei, M. Jia, J. Zhai, Z. L. Wang, Large-scale fabrication of robust textile triboelectric nanogenerators. *Nano Energy* **71**, 104605 (2020).

45. K. Chen, L. Zhang, X. Kuang, V. Li, M. Lei, G. Kang, Z. L. Wang, H. J. Qi, Dynamic photomask-assisted direct ink writing multimaterial for multilevel triboelectric nanogenerator. *Adv. Funct. Mater.* **29**, 1903568 (2019).

46. S. Wang, M. He, B. Weng, L. Gan, Y. Zhao, N. Li, Y. Xie, Stretchable and wearable triboelectric nanogenerator based on kinesio tape for self-powered human motion sensing. *Nanomaterials* **8**, 657 (2018).

47. Y.-C. Lai, J. Deng, S. Niu, W. Peng, C. Wu, R. Liu, Z. Wen, Z. L. Wang, Electric eel-skin-inspired mechanically durable and super-stretchable nanogenerator for deformable power source and fully autonomous conformable electronic-skin applications. *Adv. Mater.* **28**, 10024–10032 (2016).

48. Z. Wen, Y. Yang, N. Sun, G. Li, Y. Liu, C. Chen, J. Shi, L. Xie, H. Jiang, D. Bao, Q. Zhuo, X. Sun, A wrinkled PEDOT:PSS film based stretchable and transparent triboelectric nanogenerator for wearable energy harvesters and active motion sensors. *Adv. Funct. Mater.* **28**, 1803684 (2018).

49. J. Chen, H. Guo, X. Pu, X. Wang, Y. Xi, C. Hu, Traditional weaving craft for one-piece self-charging power textile for wearable electronics. *Nano Energy* **50**, 536–543 (2018).

50. S. Lu, L. Gao, X. Chen, D. Tong, W. Lei, P. Yuan, X. Mu, H. Yu, Simultaneous energy harvesting and signal sensing from a single triboelectric nanogenerator for intelligent self-powered wireless sensing systems. *Nano Energy* **75**, 104813 (2020).

51. Z. Zhou, X. Li, Y. Wu, H. Zhang, Z. Lin, K. Meng, Z. Lin, Q. He, C. Sun, J. Yang, Z. L. Wang, Wireless self-powered sensor networks driven by triboelectric nanogenerator for in-situ real time survey of environmental monitoring. *Nano Energy* **53**, 501–507 (2018).

52. K. Zhao, Z. L. Wang, Y. Yang, Self-powered wireless smart sensor node enabled by an ultrastable, highly efficient, and superhydrophobic-surface-based triboelectric nanogenerator. *ACS Nano* **10**, 9044–9052 (2016).

53. A. Ahmed, Z. Saadatnia, I. Hassan, Y. Zi, Y. Xi, X. He, J. Zu, Z. L. Wang, Self-powered wireless sensor node enabled by a duck-shaped triboelectric nanogenerator for harvesting water wave energy. *Adv. Energy Mater.* **7**, 1601705 (2017).

54. J. Wang, H Zhang, Y. Xie, Z. Yan, Y Yuan, L. Huang, X. Cui, M. Gao, Y. Su, W. Yang, Y. Lin, Smart network node based on hybrid nanogenerator for self-powered multifunctional sensing. *Nano Energy* **33**, 418–426 (2017).

55. Z. Lin, J. Chen, X. Li, Z. Zhou, K. Meng, W. Wei, J. Yang, Z. L. Wang, Triboelectric nanogenerator enabled body sensor network for self-powered human heart-rate monitoring. *ACS Nano* **11**, 8830–8837 (2017).

56. T. Zhao, C. Zheng, H. He, H. Guan, T. Zhong, L. Xing, X. Xue, A self-powered biosensing electronic-skin for real-time sweat Ca^{2+} detection and wireless data transmission. *Smart Mater. Struct.* **28**, 085015 (2019).